# scientific reports

OPEN

# In situ growth of luminescent d-f MOF nanostructures on bacterial cellulose as an accessible kit for early jaundice diagnosis

Arash Farahmand Kateshali[1], Faezeh Moghzi[1], Janet Soleimannejad[1✉] & Jan Janczak[2]

During the initial week after birth, a majority of newborns experience hyperbilirubinemia and jaundice as a result of the build-up of unconjugated Bilirubin (BR) in their bloodstream. If elevated BR levels are not adequately addressed, it could result in brain damage. Despite advancements in luminescence-based sensing technology for clinical purposes, there remains a significant demand for diagnostic devices with accurate, specific, portable, and affordable features. We present a luminescent nanopaper-based assay kit for visual recognition of BR. This novel kit comes with a smartphone readout, enabling effortless recognition of BR. To develop the kit, a new d – f heterometallic MOF $\{[Ce_2Zn(pzdc)_4(H_2O)_6]\cdot 2H_2O\}_n$ (pzdc = 2,3-pyrazinedicarboxylic acid) (CeZn-MOF) with advantageous photophysical features was grown on bacterial cellulose (BC) nanofibers to form BC@CeZn-MOF platform. The platform's luminescence quenches in the presence of BR with a turn-off mechanism originating from Inner Filter Energy (IFE). The luminescence quenching was linearly proportional to the concentration of BR in range of $0.1 – 20$ mg.dL$^{-1}$ (LOD = 0.027 mg.dL$^{-1}$), and recognition of small amount of BR could be attained with a smartphone camera. Furthermore, the luminescence emission of the sensing platform was recovered upon UV light (470 nm) through photo-isomerizing of BR into lumirubin as a non-PL quencher. The kit's feasibility was confirmed through validating its practicality for detecting BR in human serum samples and its compatibility with clinical procedures. The non-poisonous nature and distinctive photophysical characteristics of platform makes it an excellent choice, easy-to-use BR recognition assay kit.

**Keywords** d–f heterometallic MOF, Bacterial cellulose, Bilirubin, Smartphone-based assay kit, Point-of-care

During a baby's early days, there's a risk of elevated Bilirubin (BR) levels leading to hyperbilirubinemia, causing yellowing of skin and eyes[1,2]. BR includes water-soluble conjugated (CBR) and water-insoluble unconjugated (UBR) types. Healthy individuals have serum BR levels of $0.1–1.2$ mg.dL$^{-1}$, comprising CBR ($0.1–0.4$ mg.dL$^{-1}$) and UBR ($0.2–0.7$ mg.dL$^{-1}$). Jaundice is clinically defined as blood BR levels exceeding 2.5 mg.dL$^{[-1\ 3]}$.

The lipophilic nature of BR makes it insoluble in water, requiring hepatic conjugation in the liver for elimination[5,6]. Accumulation of unconjugated BR can lead to serious consequences, including hepatic dysfunction, mental disorders, brain damage, and even fatality, especially in newborns[7,8]. Phototherapy is employed to treat neonatal jaundice by exposing newborns to visible light, inducing the conversion of BR into lumirubin through photo-isomerization. Lumirubin, with lower toxicity and reduced albumin binding affinity, is eliminated primarily through urine, contributing to the yellow discoloration observed in jaundiced patients[9,10]. Due to these serious health concerns of untreated severe jaundice, the accurate and timely diagnosis and, consequently, early treatment of jaundice are arguably crucial. In recent years, numerous techniques have been investigated for the detection and measurement of BR as a diagnostic tool for biological disorders[11–13].

Unfortunately, these approaches require long laboratory turnaround time from sample collection to publishing test results, high volumes of sample, and sophisticated laboratory equipment with trained operators, which consequently restrict their applications to laboratories and unable to meet the requirements of an effective sensor such as instantaneous response, high selectivity and sensitivity, recyclability, and high photo-stability. Several handheld portable BR devices are available for percutaneous recognition, providing results for Point-of-

[1]School of Chemistry, College of Science, University of Tehran, P.O. Box 14155-6455, Tehran, Iran. [2]Institute of Low Temperature and Structure Research, Polish Academy of Science, 50-422 Wrocław, Poland. ✉email: jsoleimannejad@ut.ac.ir

Care Testing. However, the accuracy of these results can be influenced by the infant's skin color. Hemoglobin, a major light absorber in the dermis (particularly in the 400–425 nm and 500–600 nm) competes with BR absorption, impacting the outcome. As a result, percutaneous BR detections in newborns may not match the precision of blood-based procedures. A thorough literature survey reveals that there is still a need for the development of novel detection platforms that can effectively address the aforementioned challenges associated with the detection of BR[14–18]. Luminescence detection plays a very important role in analytical chemistry due to its visualization readout mode, fast response, operational simplicity, and very high sensitivity in a wide range of concentrations[19].

To date, very few luminescent platforms have been utilized for the detection of BR, including gold nanocluster, graphene oxide, quantum dots, and metal–organic frameworks (MOF)[20–23]. Among the mentioned platforms, the luminescence probes based on metal-organic frameworks (LMOFs) are promising candidates. These compounds, with their optical properties, adjustable porosity, large surface area and high physicochemical stability, meet the criteria of an effective sensor[24–26]. Until now, LMOFs have been employed for sensing of variety molecules, but having both great sensitivity and selectivity towards the desired analyte are still rare[27–30].

Moreover, the d–f heterometallic MOFs, featuring the intrinsic properties of d- and f-block, have potential applications in various fields such as luminescence. The d-block metal, like zinc with a $d^{10}$ electron configuration, as the closed shell metals have a lower energy level for their triplet excited state that allows for a more favorable alignment with the excited state energy level of f-block elements, leading to enhanced efficiency in sensitizing the luminescence of lanthanide ions[31–33]. Within the Ln ion series, Ce(III) stands out as an economical element that exhibits a strong inclination towards complexation with N-heterocyclic carboxylate ligands. This preference makes it an excellent choice for the construction of d–f MOFs[34–39].

Furthermore, the appealing and distinctive features of nanopaper made from bacterial cellulose (BC) have generated considerable interest in developing (bio)sensing platforms. The abundance of OH groups on steel-like nanofibres facilitates incorporation with guest materials as an excellent support host or scaffolding template[40]. BC nanofibers are created by cellulose-producing bacteria like *Gluconacetobacter xylinus* utilizing D-glucose monomers and possess an exceptionally crystalline structure with a three-dimensional (3D) network architecture of the numerous interweaved nanofibers that imparts excellent physical and chemical durability to BC[41–43]. The desirable traits of BC such as affordability, versatility, non-hazardous nature, and bio-decomposability are further complemented by the optical transparency, thermal durability, and strong mechanical and chemical integrity of BC nanopaper. These outstanding characteristics position BC as a favorably propitious matrix for the field of biosensing technology[44–50]. This research presents a novel jaundice diagnosis approach using an affordable and portable diagnostic kit with a smartphone-based color signal reader. The kit accurately monitors BR levels through a luminescent platform, which is quenched by BR, acting as an analytical signal captured by a smartphone camera and restored at specific wavelengths (Fig. 1). The study examines factors influencing the detection capability of sensing kit, evaluating attributes like specificity, sensitivity, linearity, and analysis of authentic samples for comprehensive assessment.

# Experimental
## Methods
*Blood serum samples*

Blood serum samples were from Imam Khomeini Hospital. Serum samples were collected from two healthy volunteers. The ethics committee of the laboratory of Tehran University of Medical Sciences approved all experimental protocols. Informed consent was obtained from all subjects. Research protocols were conducted under the Declaration of Helsinki and relevant guidelines and regulations of the Netherlands Code of Conduct for Research Integrity and the Academic Medical Center research code.

## Materials
The reagents utilized were of analytical reagent grade and were used without any further purification. The nanopaper was supplied by Nano Novin Polymer Co. located in Iran.

## Apparatus
The FT-IR data was obtained using an Aligent Technology Cary 360 FT-IR spectrometer within the range of 400–4000 $cm^{-1}$. UV-visible absorption measurements were performed using a PerkinElmer Lambda 650 spectrometer equipped with a 60 mm integrated sphere to obtain the absorption spectra. Emission spectra were measured using an Agilent Cary 5000 fluorescence spectrometer equipped with a 450 W Xe lamp. The majority of the luminescence spectra were recorded at room temperature. Thermogravimetric analysis (TGA) of compound was determined by using a Q500 thermal gravimetric analyzer (TA, USA) under a $N_2$ atmosphere at a heating rate of 50 °C/min from 40 to 900 °C. Surface area measurements (BET) were conducted using an ASAP 2420 gas adsorption instrument. The powder X-ray diffraction patterns (PXRD) of the products were analyzed within the 2-theta range of 5–50° using a D2 X-ray diffraction analysis (Brucker). Element analysis was carried out using a TM3000 scanning electron microscope (SEM) (Hitachi, Japan) with a SwiftED 3000 accessory (Oxford). Transmission electron microscopy (TEM) images and EDS spectra were provided using a JEOL JEM2100 (Japan). A single crystal of CeZn-MOF was mounted on a Xcalibur Atlas diffractometer with Mo Kα radiation (λ = 0.71073 Å). The *CrysAlis PRO 1.171.42.93* program was used for data reductions and cell refinements. The crystal structures were solved using the *SHELXT*-2014/5 program and refined with full-matrix least-squares methods based on $F^2$ using the *SHELXL*-2018/3 program[51]. All non-hydrogen atoms were anisotropically refined. The crystal structure of **CeZn-MOF** in the cif-format has been deposited with the Cambridge Crystallographic Data Center under the depository numbers CCDC-2,322,594.
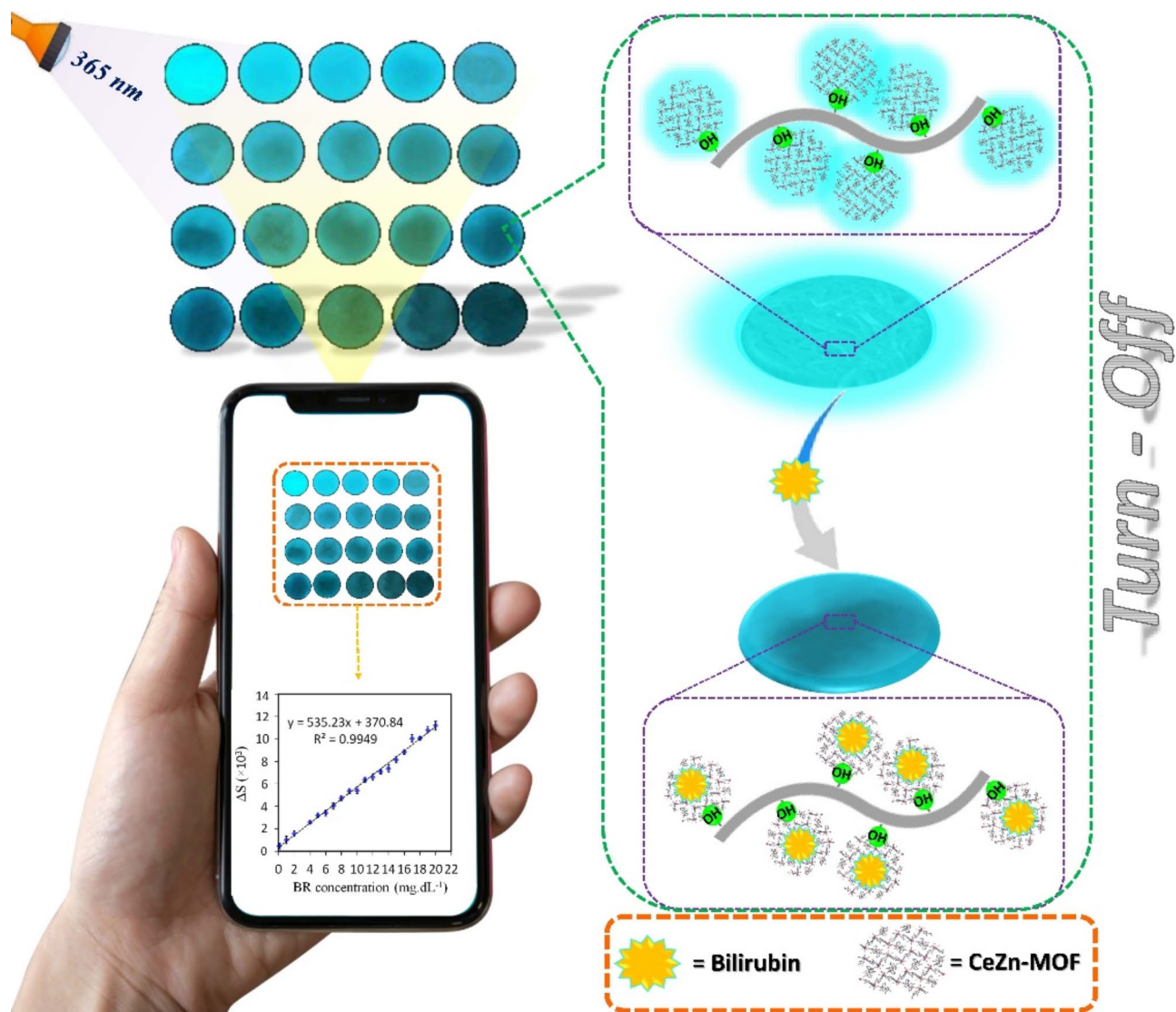
**Fig. 1**. Visualization of a BR assay kit with photoluminescent nanopaper and smartphone readout.

### Synthesis of CeZn-MOF

The hydrothermal reaction was utilized to synthesize the compound CeZn-MOF. Firstly, a mixture of $Ce(NO_3)_3.6H_2O$ (86 mg, 0.2 mmol), $Zn(NO_3)_2.6H_2O$ (60 mg, 0.2 mmol), and pzdc (67 mg, 0.4 mmol) was prepared in 8 mL water. To this 4 mL of NaOH (0.1 M) solution was added. The resulting mixture was heated at 120 °C for 24 h in a Teflon-lined stainless steel autoclave, ultimately resulting in the pale-yellow crystals. (yield; 72%) Elemental analysis (%) calcd. for $C_{24}H_{24}Ce_2N_8O_{24}Zn$: C, 24.98; H, 2.10; N, 9.71. Found (%): C, 25.30; H, 2.4; N, 10.1. Selected IR (KBr pellet, cm$^{-1}$): 3325, 2360, 1652, 1587, 1384, 1355, 1168, 1130, 1118, 896, 850, 784, 746.

### Fabrication of BC@CeZn-MOF bioplatform

To fabricate the **BC@CeZn-MOF** biosensing platform, around 100 mg of BC nanopaper was immersed in 20 mL of aqueous solution of $Ce(NO_3)_3.6H_2O$ (20 mM). To react the metal ions with the O–H groups on the surface of BC, 4 ml of NaOH solution (0.1 M) was added to the above mixture and stirred for about 15 min. In the next step, 0.2 mmol of $Zn(NO_3).6H_2O$ (60 mg) and 0.4 mmol of pzdc (67 mg) were added to the stirring mixture. The resulting mixture containing BC papers was heated at 120 °C for 24 h in a Teflon-lined stainless steel autoclave. The obtained **BC@CeZn-MOF** fabricated platform was washed three times with $H_2O$ and MeOH at room before further characterization. The mass of the synthesized MOF on the BC surface was found to be 137 mg. To optimize the amount of CeZn-MOF on BC, different concentrations of Ce(III) was utilized and in all experiments the molar ratio of 1:1:2 for Ce: Zn: pzdc and amount of BC were constant.

### Recognition of BR via BC@CeZn-MOF platform

The experiment for detecting BR concentration using the smartphone-based **BC@CeZn-MOF** platform was carried out in a series of steps. Firstly, 5 μL of different concentrations of BR solutions in the range of 0.1–20 mg.dL$^{-1}$ using a PBS buffer (pH = 7.4) were added to the fabricated platform (circles with 1 cm diameter). Then, smartphone camera images of the test zones were captured in a dark chamber under 365 nm irradiation. Subsequently, the assay sections were exposed to blue light lamps ($\lambda$ = 470 nm) for 20 min to allow for luminescence recovery. In addition, a blank sample was prepared using the same method without the addition of BR. The images were processed and analyzed using *ImageJ software* to determine the mean color intensity (in gray mode) of each test zone.

### Real sample analysis

To evaluate the clinical performance of the newly advanced smartphone-based **BC@CeZn-MOF** platforms. The small quantity of human serum samples was then processed to the proposed approach for determining the amount of BR through the **BC@CeZn-MOF** platform. The samples were diluted 5 times using a PBS buffer solution. The standard solutions of BR, with different concentrations, were added to the diluted samples to prepare real samples and 5 μL of these samples were added to the test zone and after 5 min, the images were captured in a dark chamber under 365 nm irradiation.

## Results and discussion
### Description of the crystal structure

The synthesized d-f hetero-metallic CeZn-MOF in this study is isostructure to that of the praseodymium (Pr$^{III}$) MOF previously synthesized in our group[52]. The crystal data are provided in Table S1. The asymmetric unit comprises a Ce(III) ion, a half Zn(II) ion, two pzdc$^{2-}$ ligands, three coordinated and one free H$_2$O molecule (Fig. 2a). The Ce(III) ion is surrounded by a total of nine coordinating atoms, consisting of four O atoms from four pzdc$^{2-}$ ligands, two N atoms from two pzdc$^{2-}$ rings (two different coordination modes of pzdc$^{2-}$), and three O atoms from three coordinated H$_2$O, generating a capped square antiprismatic polyhedron as shown in Fig. 2b, d. The Zn(II) ion is surrounded by two N atoms originating from two pzdc$^{2-}$ rings, while two O atoms stem from the COO$^-$ groups in the equatorial plane, and two O atoms from the COO$^-$ groups in the axial position revealing a distorted octahedral polyhedron of ZnO6 (see Fig. 2c, e).

In polymeric construction, two O atoms from COO$^-$ group with *anti – anti* fashion and one N atom from the pyrazine ring of pzdc$^{2-}$ molecules connect the Ce ions together, the Ce⋯Ce distance of 6.134 (4) Å, generating a 1D sequence of Ce-pzdc. Moreover, the pzdc$^{2-}$ ligands through one O atom of COO$^-$ group and N atom from the pyrazine ring interconnect the 1D sequences of Ce-pzdc into 2D sheets. The Zn metalloligands as 2-connector linkers play a significant role in connecting the 2D Ce-coordination layers, the Ce⋯Zn separation of 6.766 (3) Å, leading to an extended 3D network coordination construction as illustrated in Fig. 3a, b.

### Physical measurements of BC@CeZn-MOF composite

The PXRD analysis (Fig. 4a) verifies the phase integrity and the congruence between the **BC@CeZn-MOF** composite and its components. The PXRD pattern reveals distinct peaks at $2\theta \approx 8.3, 10.7, 13.7, 14.7, 16.8,$ and $18.5°$ corresponding to the characteristic diffractions of CeZn-MOF crystal planes (011), (021), (031), (002), (111), and (130), respectively, which demonstrates satisfactory conformity with the simulated pattern of the highly pure crystalline CeZn-MOF. Also, in **BC@CeZn-MOF** composite, the diffraction peaks at $2\theta \approx 14.6,$
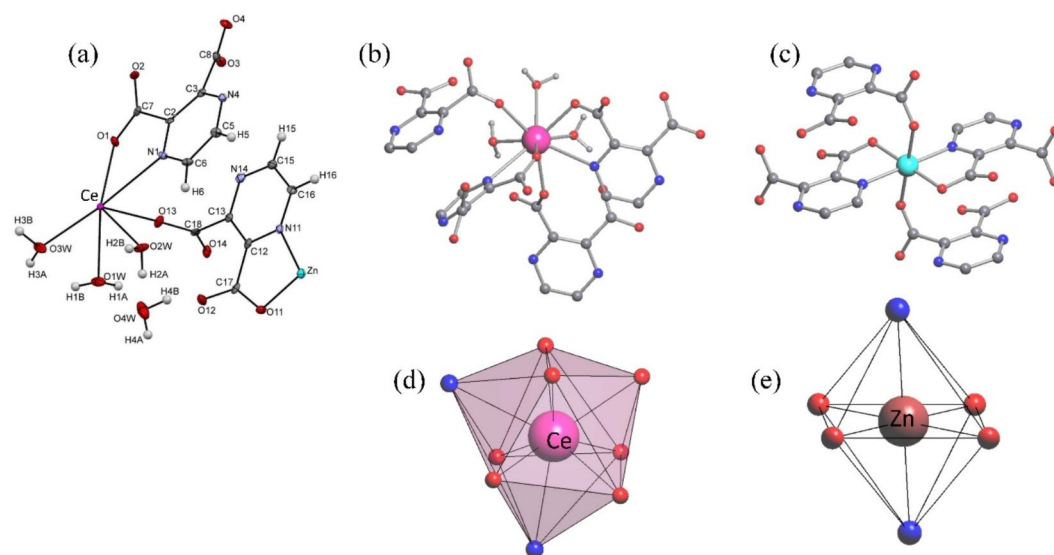


**Fig. 2**. (a) Asymmetric unit with its atom labeling scheme, (b) Coordination environment of Ce(III), (c) Coordination environment of Zn(II), (d, e) Coordination geometry of Ce and Zn atoms, respectively.
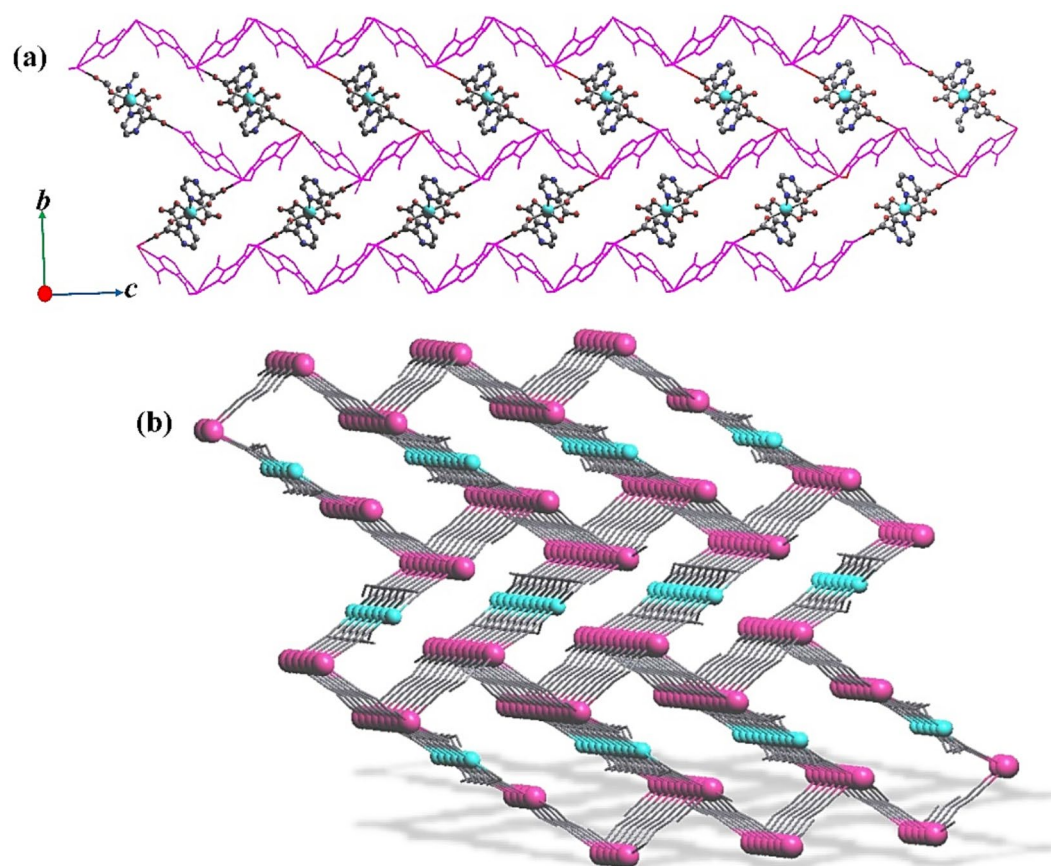
**Fig. 3**. (a) The 3D structure of CeZn-MOF and the exhibition of the Zn metallo-ligands in between 2D zigzag layers (purple), and (b) a simplified representation of the overall structure.

16.2, and 22.5° correspond to the (110), (1$\bar{1}$0), and (002) planes of BC, respectively. Therefore, the two main components of the composite, CeZn-MOF and BC, are reserved in their pristine crystalline phases, which evidences that the CeZn-MOF is embedded into the BC matrix. Additionally, to access the stability of CeZn-MOF in PBS solution, the sample was soaked in PBS for 3 days. Analysis of the PXRD patterns revealed that the framework remained stable. CeZn-MOF exhibited remarkable resistance to acids and bases, with the framework maintaining integrity within a broad pH range of 4 to 9 (refer to Fig. S1).

Figure 4b shows the FT-IR spectra of the **BC@CeZn-MOF** composite and its components. The FT-IR analysis of CeZn-MOF reveals the broadband at 3415–3321 cm$^{-1}$, indicating the presence of H$_2$O molecules. The peaks observed at around 1351 (s), 1388 (s) and 1592 (s), 1658 (s) cm$^{-1}$ are attributed to the symmetric and asymmetric vibrations of the COO$^{-}$ groups ($v_{\text{sym COO}}$ and $v_{\text{asy COO}}$), which in turn confirm the coordination of the ligand to Ce(III) center. Also the OH broad bands of CeZn-MOF and BC at 3415 and 3360 cm$^{-1}$, respectively, displayed a blue shift in the FT-IR spectrum of the **BC@CeZn-MOF** and appear at 3340 and 3285 cm$^{-1}$. The results demonstrate the existence of physical interaction between the MOF and BC and that of its contribution to the excellent compatibility of mechanical properties of the kit.

The TGA analysis of CeZn-MOF and **BC@CeZn-MOF** composite was utilized to investigate thermal stability by examining the correlation between percentage weight losses and temperature increments, as illustrated in Fig. 4c. Weight loss occurred in three distinct stages: the first between 100 and 300 °C, the second between 300 and 500 °C, and the third between 500 and 700 °C. These stages have been assigned to specific processes: the first stage involves the evaporation of both free and coordinated H$_2$O molecules, the second stage corresponds to the disintegration of the pzdc$^{2-}$ ligands, and the third and final stage entails the decomposition of the framework, resulting in the formation of CeO$_2$ and ZnO as the ultimate products. Furthermore, a pronounced weight loss in the second stage was noticeable at approximately 310 °C for **BC@CeZn-MOF**, attributed to the decomposition of the cellulose structure.

N$_2$ sorption isotherms were measured at 77 K to investigate the surface area and porosity (Fig. 4d). The sorption profile of CeZn-MOF could be classified as type I isotherm features, which shows that the CeZn-MOF framework is micro-porous. A hysteresis loop appeared at relatively high pressure, which is ascribed to the reversible uptake of nitrogen in the pores. BET surface areas of CeZn-MOF and **BC@CeZn-MOF** are 653.61 m$^2$/g and 476.28 m$^2$/g, respectively. BET surface areas of **BC@CeZn-MOF** is greater than that of bacterial cellulose (73.4 m$^2$/g) due to the loading of MOFs on BC. The calculated total pore volume of BC, CeZn-MOF and **BC@CeZn-MOF** are presented in Table 1.
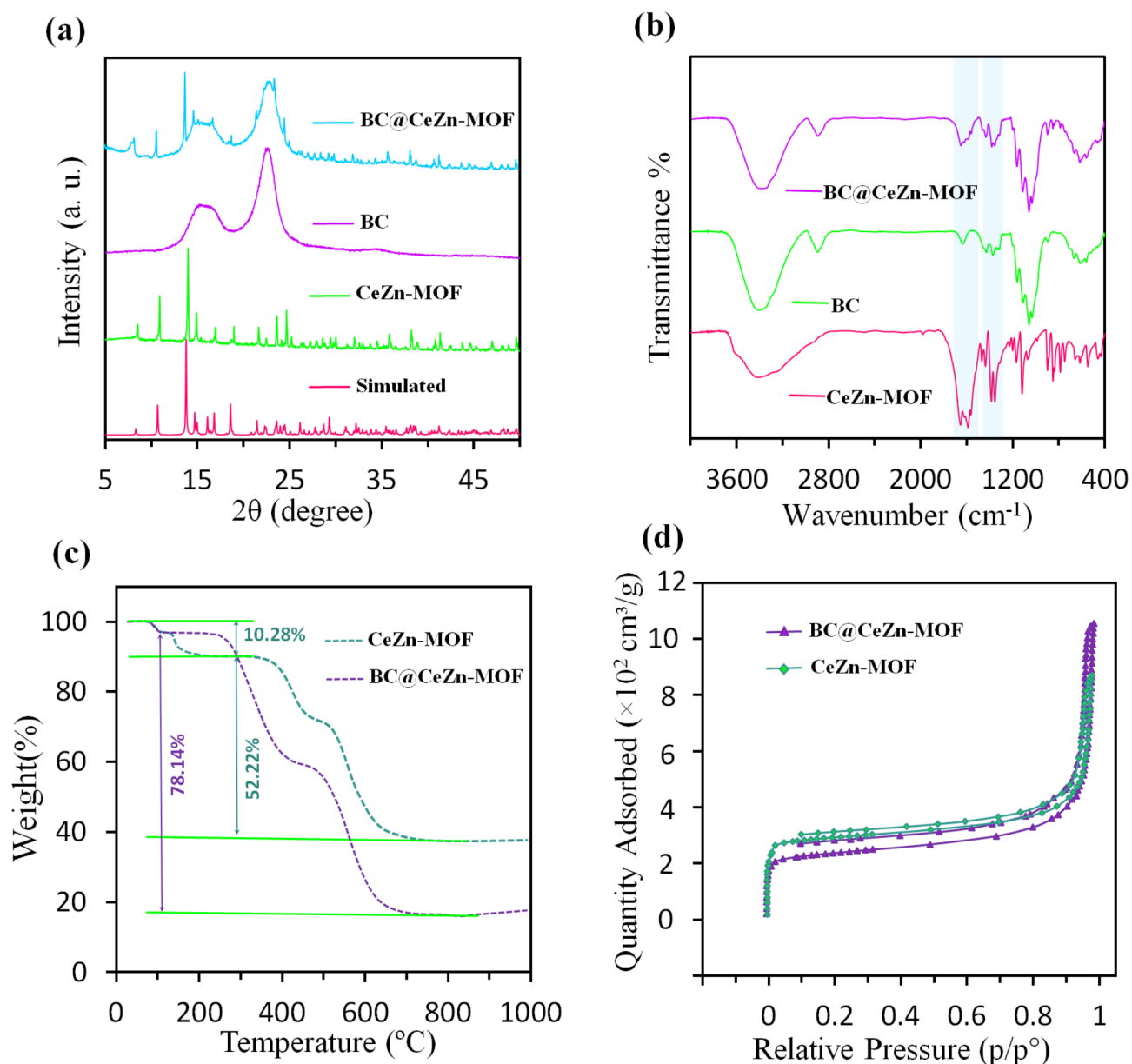
**Fig. 4**. (a) PXRD pattern of the simulated, synthesized CeZn-MOF, BC, and **BC@CeZn-MOF**, (b) FT-IR spectra of CeZn-MOF, BC, and **BC@CeZn-MOF**, (c) TGA of **CeZn-MOF**, and **BC@CeZn-MOF**, (d) BET analysis of CeZn-MOF, and **BC@CeZn-MOF**. (All analyses of **BC@CeZn-MOF** correspond to the $Ce^{3+}$ concentration of 20 mM).

| Materials | BET (m²/g) | Total pore volume (cm³/g) |
|---|---|---|
| BC | 73.4 | 0.31 |
| CeZn-MOF | 653.61 | 0.63 |
| BC@CeZn-MOF | 476.28 | 0.74 |

**Table 1**. BET surface area and total pore volume of BC, CeZn-MOF, and **BC@ CeZn-MOF**.

The Fig. 5a shows that the size of BC nanofibers and the synthesized CeZn-MOF on the surface of the BC nanofiber is less than 100 nm. The initial aim of the present study was to synthesis the CeZn-MOF on BC nanofibers with desirable uniform structure with smooth surface, highest possible surface-to-volume ratio, and highest possible available functional groups. This way, the different amount of CeZn-MOF was utilized to optimize the luminescence intensity of fabricated bio-platform. The surface SEM images of BC nanofibers and BC@CeZn-MOF platform are presented in Fig. 5. With the initial Ce(III) concentrations between 5 and 15
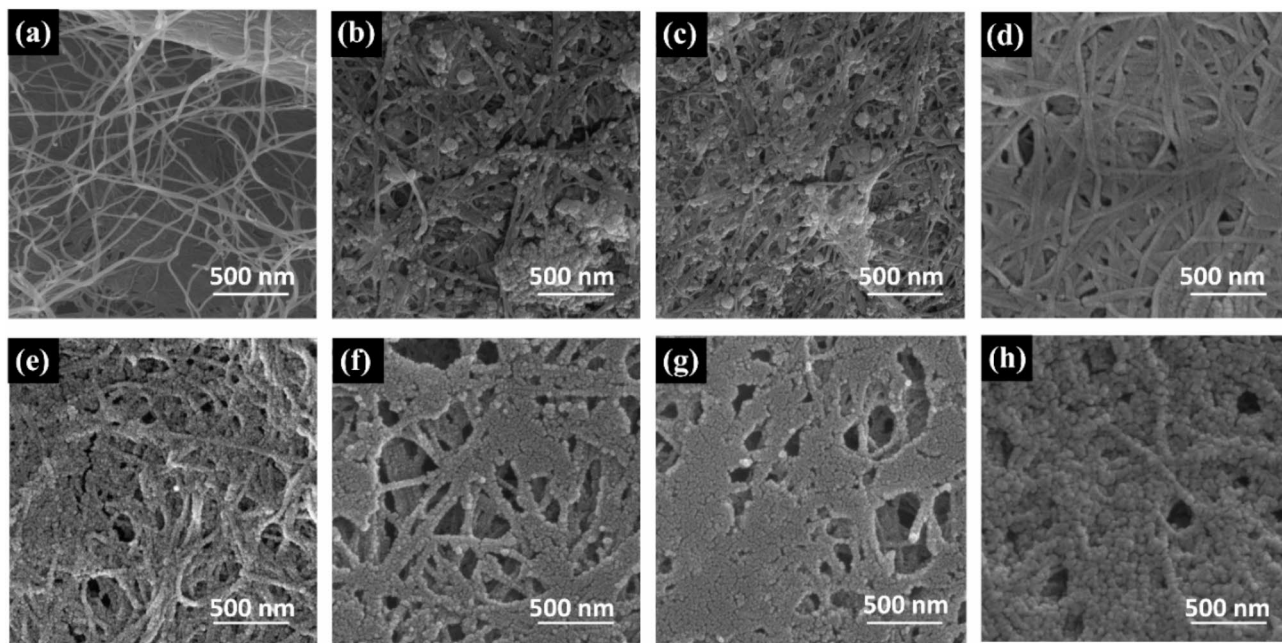
**Fig. 5**. The SEM images of (a) BC nanofibers, (b) BC with different concentrations of Ce ions: (b) 5, (c) 10, (d) 15, (e) 20, (f) 25, (g) 30, and (h) 35 mM.
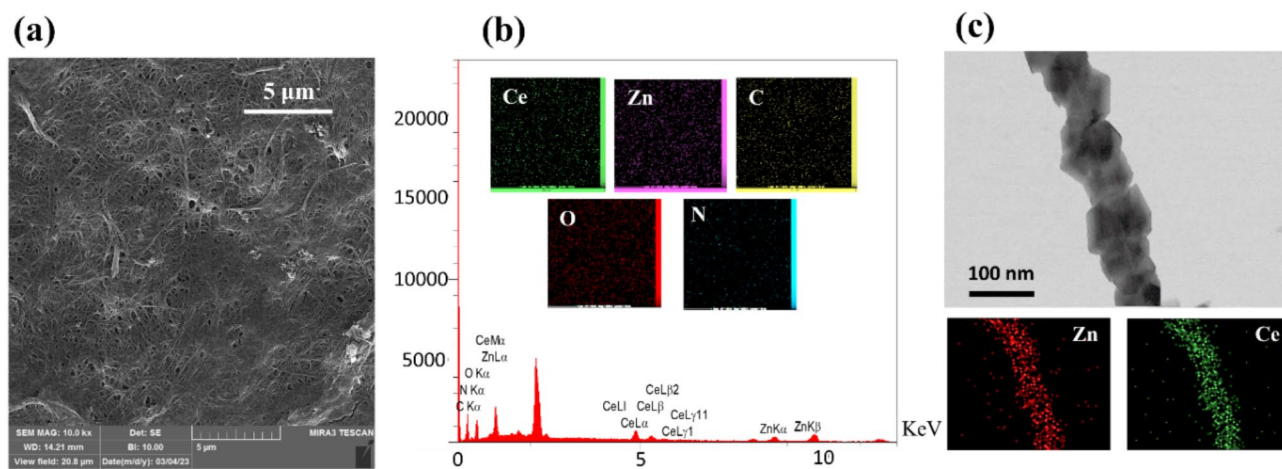


**Fig. 6**. (a) SEM image of BC@CeZn-MOF, (b) EDX spectrum; overlay elemental mapping images of **BC@ CeZn-MOF**: Ce (green), Zn (purple), N (blue), O (red), and C (yellow) elements, (c) TEM-mapping of **BC@ CeZn-MOF**.

mM, the regular beads of MOF exhibit a uniform dispersion on the BC nanofibers as a result of group linkages between the two main components. Also, with further increasing concentrations, 20 and 25 mM, more uniform MOF beads on nanofibers with higher bead densities were observed. Upon increasing Ce(III) concentrations to 35 mM, it becomes evident that the MOF particles are accumulated on the nanofibers and the size of the particles are increased (in Fig. 5b – h).

The uniform dispersion and element distribution of **BC@CeZn-MOF** were further studied by SEM and EDX mapping (Fig. 6a, b), respectively. Figure 6b indicates that the platform contains Ce (green), Zn (purple), N (blue), O (red), and C (yellow) elements, uniformly distributed in the composite. TEM micrographs **BC@CeZn-MOF** (Fig. 6c) depict that the MOFs were intimately connected to fully wrapped up BC nanofibers, which is ascribed to the electrostatic interactions and van der Waals forces induced assembly between MOFs and BC. It is worth noting that MOFs were distributed uniformly throughout the composite nanofibers based on EDX elemental mapping analysis.

## Luminescent properties of CeZn-MOF and BC@CeZn-MOF

The luminescent characteristics and performance of CeZn-MOF and **BC@CeZn-MOF** for optical sensing were assessed based on the luminescence intensity under ambient conditions. The excitation spectra and solid-state luminescence of CeZn-MOF and **BC@CeZn-MOF**, revealed a blue emission at 460 nm (in Fig. 7a, b). As shown in Fig. S2, the absorption spectra demonstrates a strong and extensive broadband in the 280 and 360 nm, which can be ascribed to the chromophores $\pi \rightarrow \pi^*$ transition of pzdc$^{2-}$ ligand and intra-configuration $4f \rightarrow 5d$ transitions of Ce(III), respectively.

This is while no ligand-specific emissions were detected in the emission spectrum. Moreover, according to growing MOF nanoscale on BC nanofiber, the nanodimension, narrow band gap, high surface area, and higher oscillator strength due to higher electron-hole overlap integral in nanoscale MOF compared to bulk are key factors of higher intensity of **BC@CeZn-MOF** compared to CeZn-MOF[53,54].

The evaluation aimed to optimize the conditions and improve the efficacy of the BR assay kit that relies on smartphones. Specifically, the effect of the quantity of CeZn-MOF on BC nanofibers and how it impacts blue light illumination were investigated. Varying Ce(III) ion concentrations between 5 and 35 were used to achieve the highest emission intensity. The experimental results show that the highest intensity of the PL signal was obtained at a Ce(III) concentration of 20 mM, which was selected for the following experiments (Fig. 8).

Furthermore, the luminescence intensity of **BC@CeZn-MOF** at various pH values in solution was examined. The fabricated sensing platform was soaked in a series of solutions with pH from 3 to 9 for five min, subsequently, luminescence emission spectra were recorded. As depicted in Fig. S3a the emission intensity of the platform remains constant across a broad range of pH.

To assess the PL stability and sensor storage of the created **BC@CeZn-MOF**, they were stored at room temperature and the corresponding PL was recorded over time. The results in Fig. S3b demonstrate that the PL intensities of the produced **BC@CeZn-MOF** remained consistent for a long period, indicating their suitability for practical applications and long-term stability.

## Performance platform for BR sensing

The effectiveness of the luminescent **BC@CeZn-MOF** platform for visually detecting BR was examined. Fig. S4a and S4b represent the emission intensity of the platform before and after the sensing process, respectively. Once different concentrations of BR were used, the fabricated platform displayed color change from blue to dark under 365 nm (Fig. 9a). The smartphone captured the corresponding luminescence photos before and after adding the different concentrations of BR. Then, the color changes were quantified using *ImageJ* software. Based on Fig. 9b, as the concentration of BR increases, there is a notable decrease in the intensity of the emission spectrum of **BC@CeZn-MOF**. There was an excellent linear relationship between the gray intensity of sensing platform and BR concentration in the range of 0.1–20 mg.dL$^{-1}$ (with a correlation coefficient (r) of $R^2 = 0.9949$), as demonstrated in Fig. 9c. The linear regression equation for BR is $\Delta S = 535.23x + 370.84$, where $\Delta S$ ($\Delta S = S - S_0$ which $S_0$ and S are signal intensities before and after adding BR, respectively) is the analytical signal and C is the BR concentration in mg. dL$^{-1}$. Thus, the value of gray intensity could be used for quantitative detection of BR.
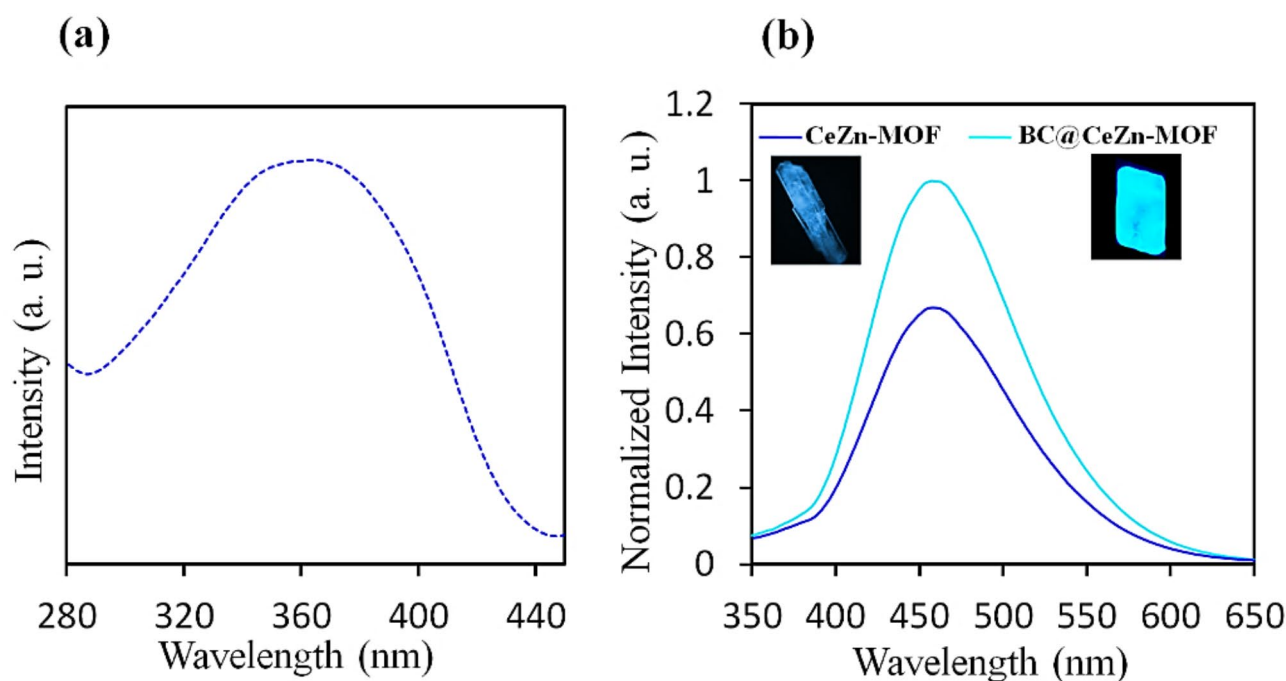


**Fig. 7**. (a) Excitation spectra of the main transitions in CeZn-MOF, (b) Emission spectra of CeZn-MOF and **BC@CeZn-MOF**, inset Fig.: blue light emission of CeZn-MOF crystal and **BC@CeZn-MOF** platform.
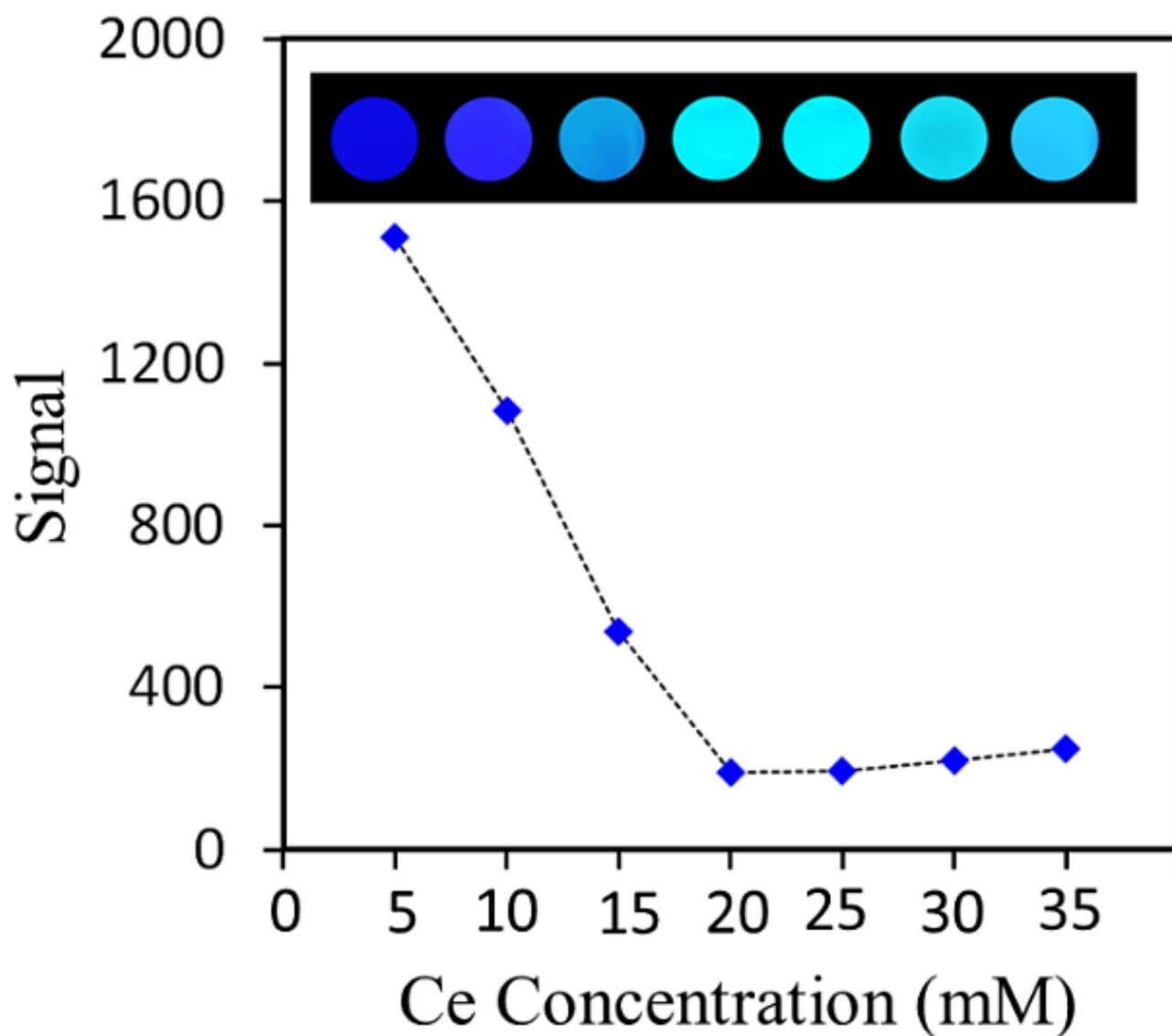
**Fig. 8**. PL intensities at different concentrations of Ce(III) ions: 5–35 mM, inset Fig.: blue emission intensity of the platforms at different concentrations of Ce(III) ions.

The LOD is estimated to be 0.027 mg.dL$^{-1}$ (0.46 μM), which is much lower than the minimum requirement of human serum.

### Interference study

To evaluate the selectivity of the fabricated **BC@CeZn-MOF** platform for the BR determination, competitive experiments were carried out at 10 mg.dL$^{-1}$ of BR in the presence of some biomolecules and metal ions. The substances including (Cl$^-$, Na$^+$, K$^+$, Ca$^{2+}$, Zn$^{2+}$, Mg$^{2+}$,), glucose (Glu), uric acid (UA), urea, L-alanine (Ala), L-ascorbic acid (AA), albumin (Alb), and cyanocobalamin were selected to record the influence, according to the recommended procedure. As shown in Fig. 10, the results demonstrate that the presence of interfering chemicals had negligible effects on the signals. This finding highlights the excellent selectivity of the smartphone-based assay kit developed for BR detection. The presence of various quenchers in blood is a common challenge when it comes to detecting specific substances. However, in this case, only BR exhibited a response to the blue light emission and underwent photo-isomerization, resulting in rearrangement. Consequently, the **BC@CeZn-MOF** analytical response remained largely unaffected by the presence of other interference species. These measurements effectively demonstrate the selectivity and robust anti-interference capability of the assay.

### Application of the method in real samples assay

To evaluate the actual applicability of the **BC@CeZn-MOF** assay kit in real samples, the platform was utilized as a sensing platform for the detection of BR in human serum samples of 5 infants and comparing the results of our
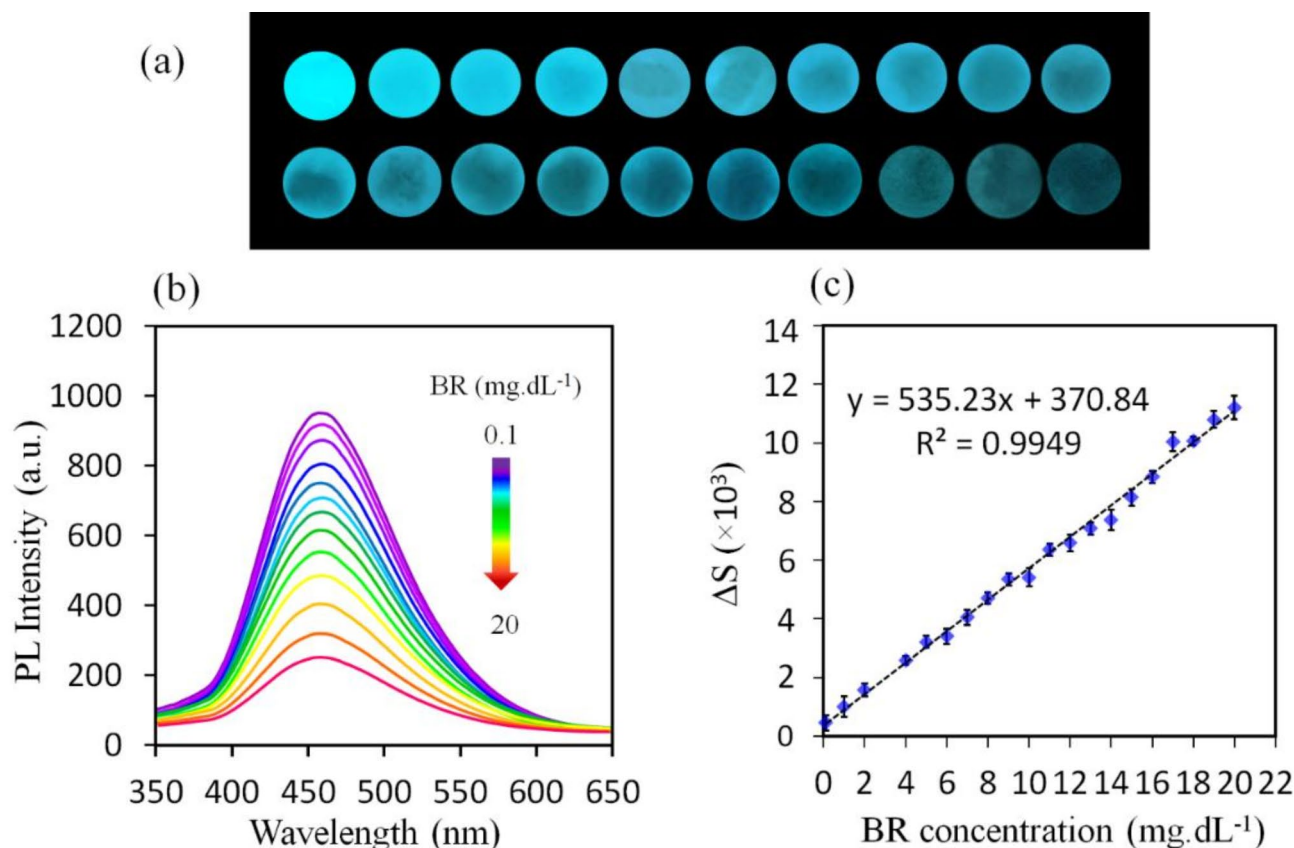
**Fig. 9**. (a) The fabricated **BC@CeZn-MOF** platforms under UV light, $\lambda = 365$ nm through increasing concentrations of BR ($0.1 - 20$ mg.dL$^{-1}$), (b) Luminescence emission intensity of **BC@CeZn-MOF** platform toward various BR concentrations, (c) Calibration plot of BR sensing using the developed smartphone assay kit in the range of $0.1 - 20$ mg.dL$^{-1}$ of BR.

developed sensor with the Audit Total BR Assay Kit (form MAN Company) as a clinical reference method for BR level detection. Fig. S5 shows the results of both methods that have been plotted against each other to compare the methods. The regression coefficient of this comparison ($r = 0.9955$) reveals the results, and the performance of our developed smartphone-based BR assay kit is comparable to reference methods that are routinely used for determination of BR level in blood samples and jaundice diagnosis in clinical laboratories. The obtained results indicate the usability of the developed smartphone-based assay kit for BR level detection at the point-of-care and also clinical laboratories.

To evaluate the practical efficacy of the luminescence platform, the standard method was employed to detect BR in human serum. The luminescence intensity was measured after diluting the real samples 5 times with PBS. The spiked BR exhibited a recovery ranging from 98 to 104%. The CeZn-MOF luminescence system exhibits good accuracy for the recognition of total BR, as illustrated by the relative standard deviation (RSD) being less than 3.3%. This indicates that the system holds promise as a reliable method. Table 2 presents the experimental results. Also, Table S2 shows a comparison of the performance of BC@CeZn-MOF platform in BR detection relative to other synthetic platforms.

### Reusability

To assess the potential reusability of **BC@CeZn-MOF** in detecting BR, the PL of the developed BR sensor is quenched in the presence of BR and then restored upon blue light ($\lambda = 470$ nm) exposure during 20 min. As shown inset Fig. 11, the blue emission light of **BC@CeZn-MOF** was quenched in the presence of 10 mg.dL$^{-1}$ of BR under $\lambda = 365$ nm irradiation, while the recovered BR selectively undergoes photo-isomerization and photo-oxidation upon exposure to UV light ($\lambda = 470$ nm), converting it into colorless oxidation products, lumirubins, acting as non-PL quencher species (as shown in Fig. S6). Furthermore, the assay kit demonstrated remarkable restoration of its initial luminescence characteristics even after undergoing three cycles of repeated luminescence detection experiments, as depicted in Fig. 11.

### Possible mechanism of the sensing system

Having confirmed the exceptional detection capability of **BC@CeZn-MOF** towards BR, delving into a comprehensive investigation of its sensing mechanism becomes imperative. This mechanism can be corroborated through the examination of spectral overlaps between MOF and BR. The emission band of CeZn-MOF exhibit
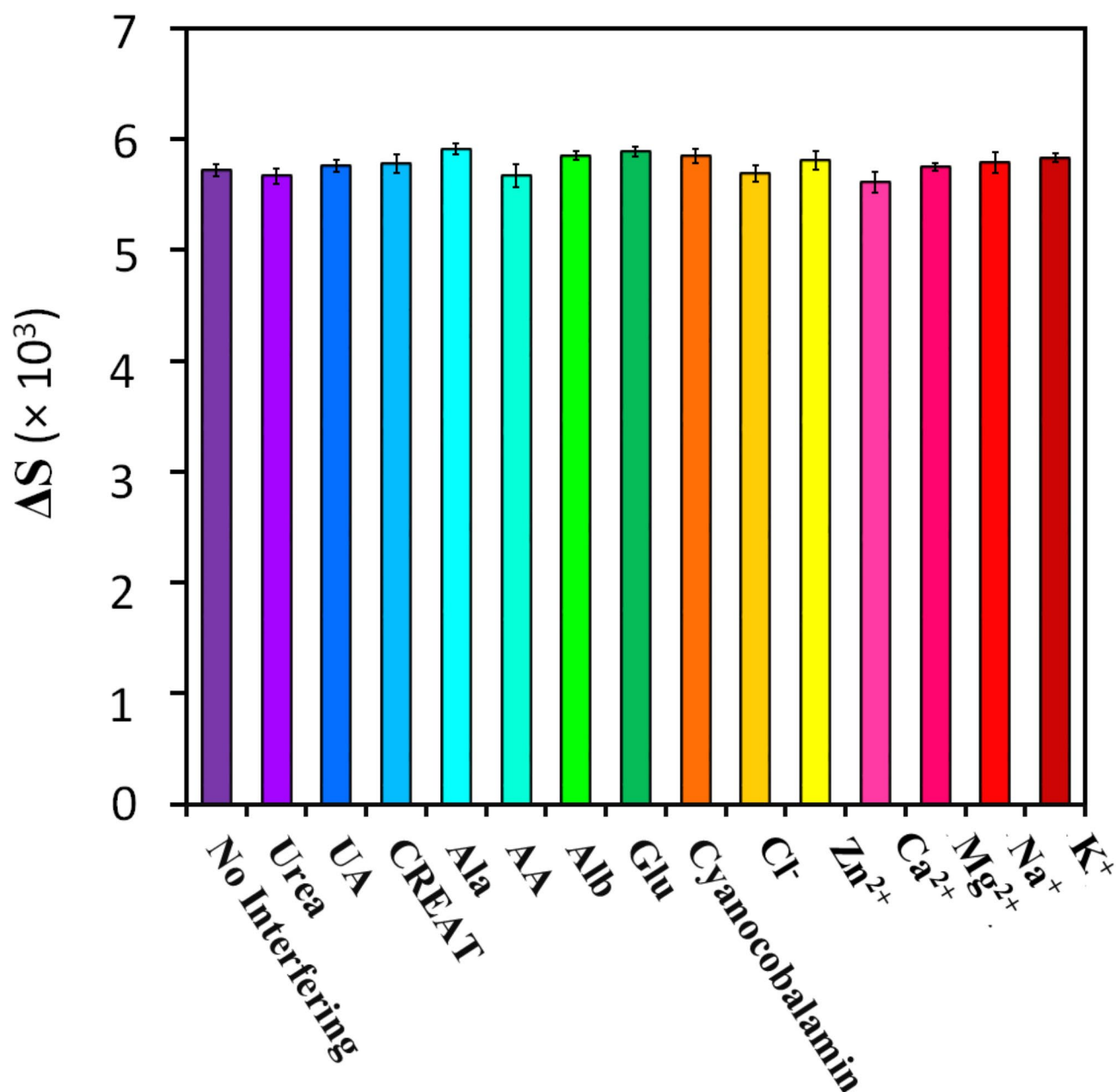
**Fig. 10**. Effect of some coexisting (bio)chemicals on the analytical response of the fabricated **BC@CeZn-MOF** toward BR sensing.

| Sample | Spiked (mg.dL$^{-1}$) | Detected (mg.dL$^-$) | RSD (% $n = 3$) | Recovery (%) |
|---|---|---|---|---|
| Human serum | 0 | 0.12 ± 0.004 | 3.3 | - |
| | 1 | 1.1 ± 0.023 | 2.1 | 98 |
| | 2 | 2.16 ± 0.046 | 2.1 | 102 |
| | 3 | 3.21 ± 0.076 | 2.3 | 103 |
| | 4 | 4.09 ± 0.099 | 2.4 | 99 |
| | 5 | 5.31 ± 0.084 | 1.6 | 104 |

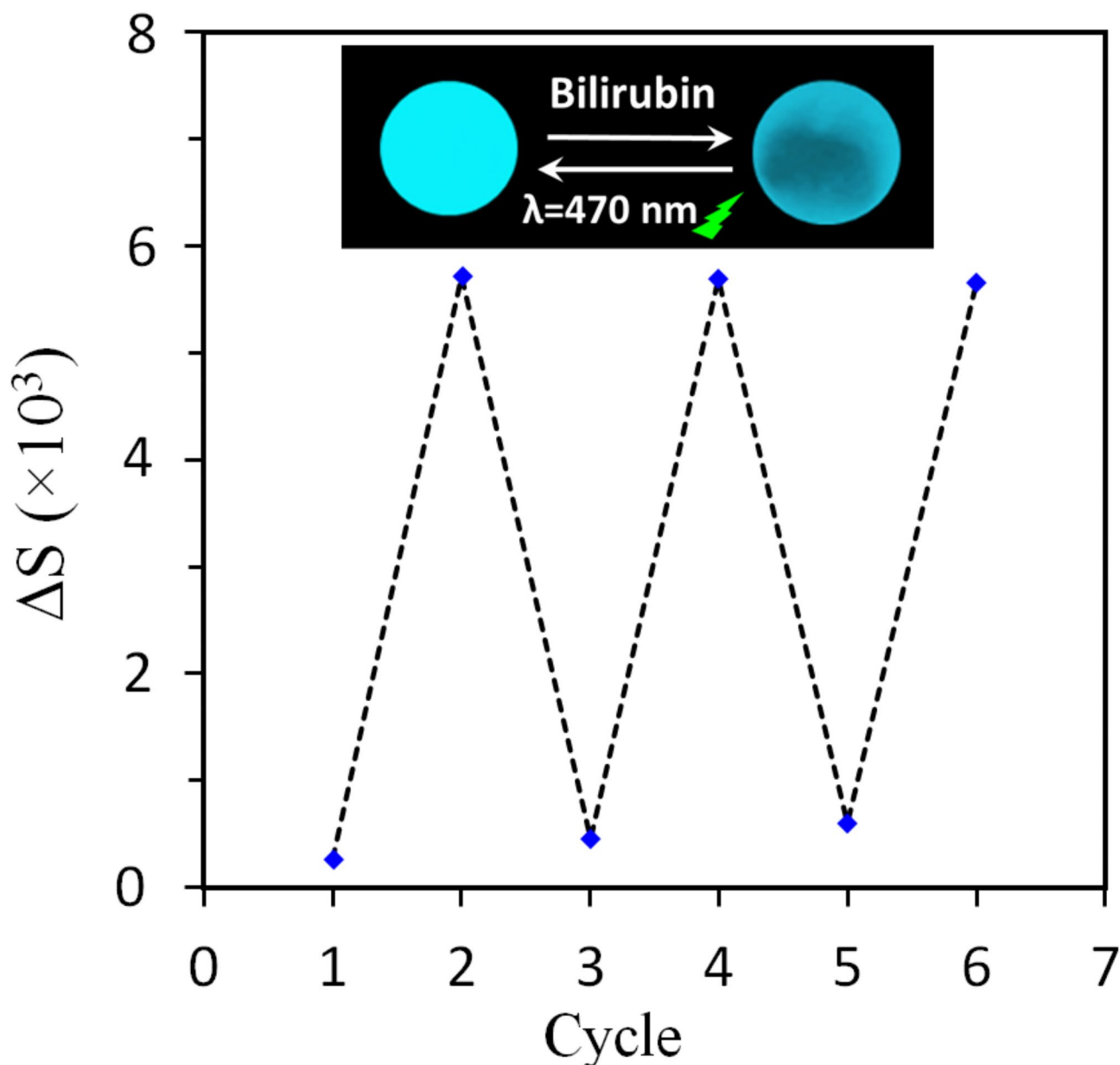**Table 2**. Recognition of total BR in real samples.

**Fig. 11**. The correlation between emission intensity ratio of the sensing platform and cycles. Inset: quenching and recovering luminescence intensity of **BC@CeZn-MOF** composite under λ = 365 and 470 nm, respectively, in presence of BR.

a significant overlap with the absorbance spectrum of BR (Fig. 12a) indicative of IFE, the phenomenon in which an excited donor transfers energy to an acceptor group through a non-radiative process, occurring between the two species[55–57]. To provide a comprehensive illustration of the quenching process, an analysis of time-resolved luminescence decay was conducted both in the absence and presence of BR as depicted in Fig. 12b, the luminescence lifetime of MOF ($\tau_{CeZn-MOF}$) exhibited a reduction from 0.38 μs to 0.21 μs upon the introduction of BR ($\tau_{MOF + BR}$). The outcome verifies that the luminescence quenching observed in CeZn-MOF upon BR interaction is primarily attributed to a static quenching effect[58–60]. Moreover, the restoration of luminescence can be attributed to the intrinsic photo-isomerization of BR under specific light conditions with a wavelength of λ = 470 nm. In this process, the bridging exocyclic double bond in each of the two dipyrrinones of BR adopts a Z configuration, resulting in the formation of lumirubins structure as a non-photoluminescence quencher. This leads to a distinct enhancement of the PL signal.

## Conclusions
To summarize, this contribution has successfully introduced a novel smartphone-based diagnostic bio-platform that is user-friendly, affordable, safe, and portable. This kit allows for the diagnosis of jaundice by visually determining the levels of BR in real samples. An innovative luminescent assay kit using **BC@CeZn-MOF**
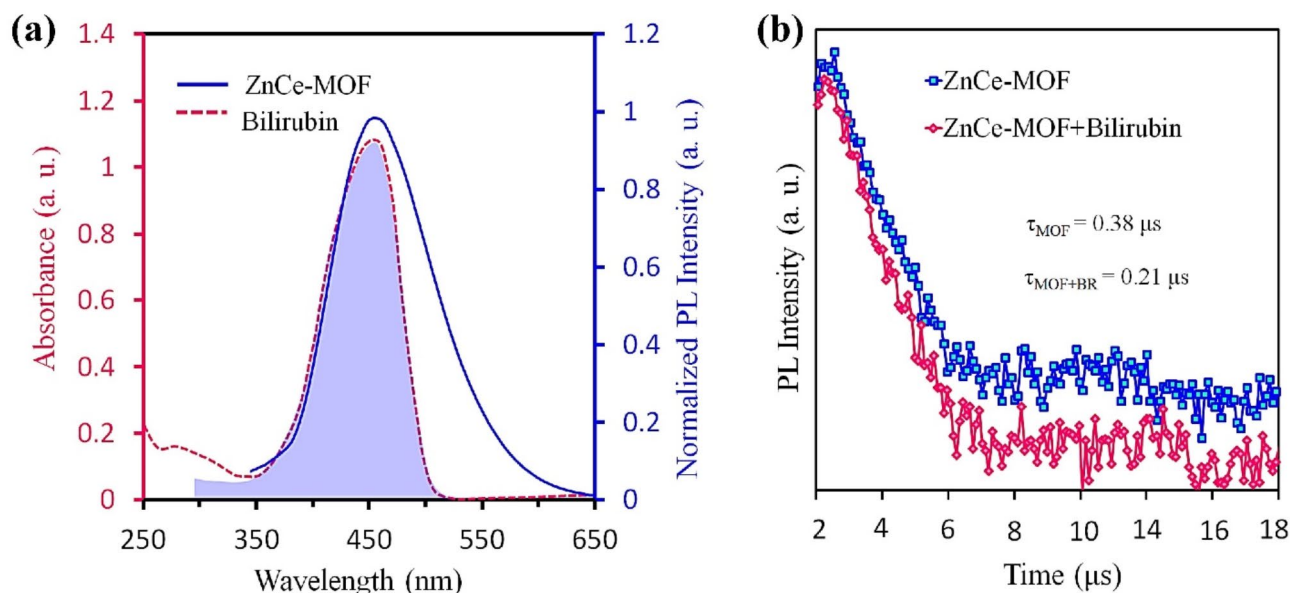
**Fig. 12**. (a) Overlap of emission spectra of CeZn-MOF and absorbance spectra of BR, (b) Time-resolved decay curves of MOF and MOF + BR in the absence and presence of BR.

composite coupled with smartphone technology was successfully designed, enabling highly sensitive and specific detection of BR. Furthermore, the luminescence sensing probe can be effectively quenched in the presence of BR due to the overlapping absorption band of BR and PL of the platform *via* IFE quenching mechanisms. It is important that the developed assay kit can also be considered as a green recognition platform because of uses BC nanopaper as non-venomous, affordable, environmentally material, and reduces the need for excessive sample collection. Moreover, the present platform demonstrates notable characteristics such as remarkable sensitivity, and excellent selectivity in detecting BR and displayed ultra-fast response (0.21 µs) with a low detection limit (0.027 mg.dL$^{-1}$). It stands out as the luminescent platform based on lanthanide MOF that overcomes interference from other biomolecules and metal ions in human serum samples. Additionally, the usability strategy for detecting BR in the developed smartphone-based assay kit relied on selectively recovering the quenched PL of **BC@CeZn-MOF** platform when exposed to blue light ($\lambda = 470$ nm). This recovery is attributed to the photo-isomerization of BR to lumirubins isomer. The finding reveals that the successfully fabricated lanthanide-based diagnostic bioplatform has demonstrated significant potential as a robust sensing tool for detecting BR in point-of-care settings and routine clinical medicine.

## Data availability

The datasets used and analysed during the current study are available from the corresponding author on request.

## References

1. Qattea, I., Farghaly, M. A., Elgendy, M., Mohamed, M. A. & Aly, H. Neonatal hyperbilirubinemia and bilirubin neurotoxicity in hospitalized neonates: analysis of the US database. *Pediatr. Res.* **91**, 1662–1668 (2022).
2. Hegyi, T. & Kleinfeld, A. Neonatal hyperbilirubinemia and the role of unbound bilirubin. *J. Maternal-Fetal Neonatal Med.* **35**, 9201–9207 (2022).
3. Ngashangva, L., Bachu, V. & Goswami, P. Development of new methods for determination of bilirubin. *J. Pharm. Biomed. Anal.* **162**, 272–285 (2019).
4. Karim, R., Zaman, M. & Yong, W. H. A Non-invasive methods for neonatal jaundice detection and monitoring to assess bilirubin level: A review. *Annals Emerg. Technol. Comput. (AETiC)* **7** (2023).
5. Okwundu, C.I. & Sain, S. S. Noninvasive methods for bilirubin measurements in newborns: A report. Seminars in Perinatology. **45**, 151355 (2021).
6. Cui, Y., Wu, C., Li, L., Li, C. & Yin, S. Toward nanotechnology-enabled application of bilirubin in the treatment and diagnosis of various civilization diseases. *Mater. Today Bio* 100658 (2023).
7. Creeden, J. F., Gordon, D. M., Stec, D. E. & Hinds, T. Jr D. Bilirubin as a metabolic hormone: the physiological relevance of low levels. *Am. J. Physiology-Endocrinology Metabolism*. **320**, E191–E207 (2021).
8. Vitek, L., Hinds, T. D., Stec, D. E. & Tiribelli, C. The physiology of bilirubin: health and disease equilibrium. *Trends Mol. Med.* **29**, 315–328 (2023).
9. Uchida, Y. et al. Noninvasive monitoring of bilirubin photoisomer excretion during phototherapy. *Sci. Rep.* **12**, 11798 (2022).
10. Jazayeri, Z., Sajadi, M., Dalvand, H. & Zolfaghari, M. Comparison of the effect of foot reflexology and body massage on physiological indicators and bilirubin levels in neonates under phototherapy. *Complement. Ther. Med.* **59**, 102684 (2021).
11. Shapiro, S. M. & Riordan, S. M. Review of bilirubin neurotoxicity II: preventing and treating acute bilirubin encephalopathy and Kernicterus spectrum disorders. *Pediatr. Res.* **87**, 332–337 (2020).

12. Riordan, S. M. & Shapiro, S. M. Review of bilirubin neurotoxicity I: molecular biology and neuropathology of disease. *Pediatr. Res.* **87**, 327–331 (2020).

13. Žiberna, L., Jenko-Pražnikar, Z. & Petelin, A. Serum bilirubin levels in overweight and obese individuals: the importance of anti-inflammatory and antioxidant responses. *Antioxidants* **10**, 1352 (2021).

14. Rawal, R. et al. A comprehensive review of bilirubin determination methods with special emphasis on biosensors. *Process Biochem.* **89**, 165–174 (2020).

15. Narwal, V. et al. Bilirubin detection by different methods with special emphasis on biosensing: A review. *Sens. Bio-Sensing Res.* **33**, 100436 (2021).

16. Lu, Z. J. et al. Non-enzymatic free bilirubin electrochemical sensor based on ceria nanocube. *Sens. Actuators B.* **329**, 129224 (2021).

17. Zhang, C. et al. An effective enzymatic assay for pH selectively measuring direct and total bilirubin concentration by using of CotA. *Biochem. Biophys. Res. Commun.* **547**, 192–197 (2021).

18. Althnian, A., Almanea, N. & Aloboud, N. Neonatal jaundice diagnosis using a smartphone camera based on eye, skin, and fused features with transfer learning. *Sensors* **21**, 7038 (2021).

19. Qin, J., Wang, W., Gao, L. & Yao, S. Q. Emerging biosensing and transducing techniques for potential applications in point-of-care diagnostics. *Chem. Sci.* **13**, 2857–2876 (2022).

20. Borse, S., Murthy, Z. V. P., Park, T. J. & Kailasa, S. K. Lysozyme-decorated gold and molybdenum bimetallic nanoclusters for the selective detection of bilirubin as a jaundice biomarker. *ACS Appl. Nano Mater.* **4**, 11949–11959 (2021).

21. Zhao, W. et al. Multi-dimensional plasmonic coupling system for efficient enrichment and ultrasensitive label-free SERS detection of bilirubin based on graphene oxide-Au nanostars and Au@ ag nanoparticles. *J. Colloid Interface Sci.* **646**, 872–882 (2023).

22. Nandi, N., Gaurav, S., Sarkar, P., Kumar, S. & Sahu, K. Multifunctional N-doped carbon Dots for bimodal detection of bilirubin and vitamin B12, living cell imaging, and fluorescent ink. *ACS Appl. Bio Mater.* **4**, 5201–5211 (2021).

23. Sharifi, A. R., Naghdi, T., Yousefi, H., Kiani, M. A. & Golmohammadi, H. Nanopapers toward green photonic and optical applications. *ACS Sustain. Chem. Eng.* **10**, 16995–17026 (2022).

24. Wang, X. et al. Lanthanide MOF-based luminescent sensor arrays for the detection of castration-resistant prostate cancer curing drugs and biomarkers. *Chem. Sci.* **15**, 6488–6499 (2024).

25. Shen, X. & Yan, B. Photofunctional hybrids of lanthanide functionalized bio-MOF-1 for fluorescence tuning and sensing. *J. Colloid Interface Sci.* **451**, 63–68 (2015).

26. Ma, Y., Aierken, A., Wang, Y. & Meijerink, A. Dual functionality luminescence thermometry with Gd2O2S:Eu3+,Nd3 + and its multiple applications in biosensing and in situ temperature measurements. *J. Colloid Interface Sci.* **638**, 640–649 (2023).

27. Li, B. et al. Recent advances in molecular logic gate chemosensors based on luminescent metal organic frameworks. *Dalton Trans.* **50**, 14967–14977 (2021).

28. Jia, C., He, T. & Wang, G. M. Zirconium-based metal-organic frameworks for fluorescent sensing. *Coord. Chem. Rev.* **476**, 214930 (2023).

29. Moghzi, F., Soleimannejad, J., Sañudo, E. C. & Janczak, J. Dopamine sensing based on ultrathin fluorescent metal–organic nanosheets. *ACS Appl. Mater. Interfaces.* **12**, 44499–44507 (2020).

30. Wu, H. et al. Gelatinous lanthanide coordination polymer with aggregation-enhanced antenna effect for ratiometric detection of endogenous alkaline phosphatase. *J. Colloid Interface Sci.* **645**, 338–349 (2023).

31. Wang, L. B. et al. Highly selective detecting aspartic acid, detecting ornidazole and information encryption and decryption supported by a heterometallic anionic cd (II)-K (I)-MOF. *Spectrochim. Acta Part A Mol. Biomol. Spectrosc.* **265**, 120340 (2022).

32. You, Z. X. et al. Cage bismuth Metal–Organic framework materials based on a flexible Triazine–Polycarboxylic acid: subgram synthesis, application for sensing, and white light tuning. *Inorg. Chem.* **61**, 13893–13914 (2022).

33. Jiang, M. Y. et al. A novel d-f heterometallic CdII-EuIII Metal-organic framework as a sensitive luminescent sensor for the dual detection of ronidazole and 4-Nitrophenol. *Z. Für Anorganische Und Allgemeine Chemie.* **646**, 268–274 (2020).

34. Zhang, Q., Lei, M., Yan, H., Wang, J. & Shi, Y. A water-stable 3D luminescent Metal–Organic framework based on heterometallic [EuIII6ZnII] clusters showing highly sensitive, selective, and reversible detection of ronidazole. *Inorg. Chem.* **56**, 7610–7614 (2017).

35. Kateshali, A. F., Dogaheh, S. G., Soleimannejad, J. & Blake, A. J. Structural diversity and applications of Ce (III)-based coordination polymers. *Coord. Chem. Rev.* **419**, 213392 (2020).

36. Wan, K., Gao, Y., Chen, Z. & Li, F. A highly efficient luminescent cerium (III) coordination complex with pure-blue emission. *Dyes Pigm.* **211**, 111067 (2023).

37. Wang, A. et al. Seven Ln (III) coordination polymers with two kinds of geometric coordination but the same 3D topological property: luminescence sensing and magnetic property. *Dalton Trans.* **51**, 12324–12333 (2022).

38. Tan, B., Li, Z. W., Wu, Z. F. & Huang, X. Y. A cerium organic framework with {Cu2I2} cluster and {Cu2I2} N chain modules: structure and fluorescence sensing properties. *Sensors* **23**, 2420 (2023).

39. Zhao, Z. et al. Efficient rare Earth cerium (III) complex with nanosecond d–f emission for blue organic light-emitting diodes. *Natl. Sci. Rev.* **8**, nwaa193 (2021).

40. van Gent, J. & Roig, A. Ce 1−x Zr X O 2 nanoparticles in bacterial cellulose, bio-based composites with self-regenerating antioxidant capabilities. *Nanoscale* **15**, 13018–13024 (2023).

41. Barhoum, A. et al. Plant celluloses, hemicelluloses, lignins, and volatile oils for the synthesis of nanoparticles and nanostructured materials. *Nanoscale* **12**, 22845–22890 (2020).

42. Ma, X., Lou, Y., Chen, X. B., Shi, Z. & Xu, Y. Multifunctional flexible composite aerogels constructed through in-situ growth of metal-organic framework nanoparticles on bacterial cellulose. *Chem. Eng. J.* **356**, 227–235 (2019).

43. Abdelhamid, H. N. & Mathew, A. P. Cellulose–metal organic frameworks (CelloMOFs) hybrid materials and their multifaceted applications: A review. *Coord. Chem. Rev.* **451**, 214263 (2022).

44. Li, D. et al. Multifunctional adsorbent based on metal-organic framework modified bacterial cellulose/chitosan composite aerogel for high efficient removal of heavy metal ion and organic pollutant. *Chem. Eng. J.* **383**, 123127 (2020).

45. Liu, W. et al. Bacterial cellulose-based composite scaffolds for biomedical applications: a review. *ACS Sustain. Chem. Eng.* **8**, 7536–7562 (2020).

46. Zhou, S. et al. Cellulose Nanofiber@ conductive metal–organic frameworks for high-performance flexible supercapacitors. *ACS Nano.* **13**, 9578–9586 (2019).

47. Fan, M. et al. Bacterial-cellulose-reinforced graphite nanoplate films for electromagnetic interference shielding, heat conduction, and joule heating. *ACS Appl. Nano Mater.* **6**, 10202–10212 (2023).

48. Sun, Y., Li, X., Li, D., Ke, H. & Wei, Q. Eco-friendly sorbent of bacterial cellulose/metal–organic framework composite membrane for effective bisphenol a removal. *J. Ind. Text.* **51**, 2426S–2443S (2022).

49. Li, H., Zhang, S., Zhou, S., Cao, X. & Zheng, Y. Crystalline size effect on the energy transfer from Mo–O groups to Eu3 + ions in R2MoO6: Eu (R=La, Gd, and Y) crystals. *J. Phys. Chem. C.* **113**, 13115–13120 (2009).

50. Farahmand Kateshali, A., Moghzi, F., Soleimannejad, J. & Janczak, J. Bacterial cellulose–based MOF hybrid as a sensitive switch off–on luminescent sensor for the selective recognition of l-histidine. *Inorg. Chem.* (2024).

51. Usón, I. & Sheldrick, G. M. An introduction to experimental phasing of macromolecules illustrated by SHELX; new Autotracing features. *Acta Crystallogr. Sect. D: Struct. Biology.* **74**, 106–116 (2018).

52. Moghzi, F., Soleimannejad, J., Emadi, H. & Janczak, J. 0D to 3D PrIII metal–organic networks crystal engineered for optimal iodine adsorption. *Acta Crystallogr. Sect. B: Struct. Sci. Cryst. Eng. Mater.* **76**, 779–788 (2020).

53. Gupta, S. K., Sudarshan, K., Srivastava, A. & Kadam, R. Visible light emission from bulk and nano SrWO4: possible role of defects in photoluminescence. *J. Lumin.* **192**, 1220–1226 (2017).
54. Ren, K., Guo, X. F., Tang, Y. J., Huang, B. H. & Wang, H. Size-controlled synthesis of metal–organic frameworks and their performance as fluorescence sensors. *Analyst* **145**, 7349–7356 (2020).
55. Xia, C. et al. A selective and sensitive fluorescent probe for bilirubin in human serum based on europium (III) post-functionalized Zr (IV)-Based MOFs. *Talanta* **212**, 120795 (2020).
56. Zhao, Y., Zeng, H., Zhu, X. W., Lu, W. & Li, D. Metal–organic frameworks as photoluminescent biosensing platforms: mechanisms and applications. *Chem. Soc. Rev.* **50**, 4484–4513 (2021).
57. Rahman, M. & Harmon, H. J. Absorbance change and static quenching of fluorescence of meso-tetra (4-sulfonatophenyl) porphyrin (TPPS) by trinitrotoluene (TNT). *Spectrochim. Acta Part A Mol. Biomol. Spectrosc.* **65**, 901–906 (2006).
58. Zu, F. et al. The quenching of the fluorescence of carbon Dots: a review on mechanisms and applications. *Microchim. Acta.* **184**, 1899–1914 (2017).
59. Mohan, N., Sreejith, S., Begum, P. S. & Kurup, M. P. Dual responsive salen-type schiff bases for the effective detection of L-arginine via a static quenching mechanism. *New J. Chem.* **42**, 13114–13121 (2018).
60. Anand, S. K., Mathew, M. R. & Kumar, K. G. A dual channel optical sensor for biliverdin and bilirubin using glutathione capped copper nanoclusters. *J. Photochem. Photobiol., A.* **418**, 113379 (2021).

## Acknowledgements

## Author contributions

Arash Farahmand Kateshali: Writing – original draft, Investigation, Visualization, Validation, Formal analysis, Data curation, Conceptualization. Faezeh Moghzi: Writing – review & editing, Investigation, Visualization, Validation, Formal analysis, Data curation, Conceptualization.Janet Soleimannejad: Writing – review & editing, Project administration, Supervision. Jan Janczak: Writing – review & editing, Formal analysis.

## Declarations

## Competing interests

The authors declare no competing interests.

## Additional information

**Supplementary Information** The online version contains supplementary material available at https://doi.org/10.1038/s41598-025-94147-2.

**Correspondence** and requests for materials should be addressed to J.S.

**Reprints and permissions information** is available at www.nature.com/reprints.

**Publisher's note** Springer Nature remains neutral with regard to jurisdictional claims in published maps and institutional affiliations.